Title

Evidence for multiple early impacts on the H chondrite parent body from electron backscatter diffraction analysis

Journal

Meteoritics and Planetary Science, 58(4)

ISSN

1086-9379

Authors

Goudy, Secana P

Telus, Myriam

Chapman, Brendan

Publication Date

2023-04-01

DOI

10.1111/maps.13969

The Meteoritical Society

Meteoritics & Planetary Science 58, Nr 4, 501–515 (2023)
doi: 10.1111/maps.13969

Evidence for multiple early impacts on the H chondrite parent body from electron backscatter diffraction analysis

Secana P. GOUDY[1], Myriam TELUS[1]*, and Brendan CHAPMAN[2]

[1]Earth and Planetary Sciences, University of California, Santa Cruz, Santa Cruz, California, USA
[2]School of Earth and Space Exploration, Arizona State University, Tempe, Arizona, USA
*Corresponding author.
Myriam Telus, Earth and Planetary Sciences, University of California, Santa Cruz, CA 95064, USA.
E-mail: mtelus@ucsc.edu

(Received 16 June 2022; revision accepted 21 February 2023)

Abstract–We examined H4 chondrites Beaver Creek, Forest Vale, Quenggouk, Ste. Marguerite, and Sena with the electron backscatter diffraction (EBSD) techniques of Ruzicka and Hugo (2018) to determine if there is evidence for shock metamorphism consistent with the previously inferred histories of their early impact excavation or lack thereof. We find that all samples have EBSD data consistent with a history of synmetamorphic impact shock (i.e., shock during thermal metamorphism), followed by postshock annealing. Petrographic analysis of Sena, Quenggouk, and Ste. Marguerite found exsolved Cu and irregular troilite within Fe metal, features consistent with shock metamorphism. All samples have a spatial variability in grain deformation consistent with shock processes, though Forest Vale, Quenggouk, and Ste. Marguerite may have relict signatures of accretional deformation as indicated by variability in their olivine deformation metrics. Within the context of previous workers' geochemical observations, a more complex history is inferred for each sample. The "slow-cooled" samples, Quenggouk and Sena, were subject to synmetamorphic shock without excavation and annealed at depth. The same is true of the "fast-cooled" samples, Beaver Creek, Forest Vale, and Ste. Marguerite. However, after annealing, these rocks were excavated by a secondary impact or impacts around 5.2–6.5 Ma post-CAI formation and were left to cool rapidly on the surface of the H chondrite parent body. These interpreted histories are best compatible with a model of an impact-battered but intact onion shell for the earliest history of the H parent body. However, the EBSD evidence does not preclude a parent body disruption after 7 Ma post-CAI formation.

INTRODUCTION

The early history of the H chondrite parent body is complex and remains an open question. Discussion on the topic has primarily centered around two model types: (1) an undisrupted onion shell (Archer et al., 2019; Hellmann et al., 2019; Henke et al., 2012; Trieloff et al., 2003) and (2) disruption by an impact followed by reaccretion as a rubble pile (Blackburn et al., 2017; Davison et al., 2013; Ganguly et al., 2013, 2016; Kessel et al., 2007; Lucas et al., 2020; Ream, 2019; Taylor et al., 1987). The first of these models, that of the onion shell, envisions concentric layers of different metamorphic grades, with type 3 material at the surface and increasing in type toward the center of the body. In this model, the deeper, more metamorphosed layers spend longer durations at peak temperature and possibly reached higher temperatures than the lower grade outer layers (i.e., Monnereau et al., 2013). In the rubble pile model, the evolution of the parent body proceeds initially as it had for the onion shell model, but a large impact disrupts the body during metamorphism, mixing together material of differing metamorphic grades and histories and cooling some material as the body reaccretes as a rubble pile.

Arguments for and against each of these models have thus far been based on radiogenic geochronology and diffusive geothermometry, which have been used to infer

thermal histories for the H chondrite parent body (Archer et al., 2019; Blackburn et al., 2017; Ganguly et al., 2013, 2016; Guignard & Toplis, 2015; Harrison & Grimm, 2010; Hellmann et al., 2019; Kessel et al., 2007; Lucas et al., 2020; Ream, 2019; Scott et al., 2014; Taylor et al., 1987; Telus et al., 2014; Trieloff et al., 2003). By these methods, many samples display an inverse correlation between cooling rate and metamorphic grade that is consistent with computer-modeled onion shell thermal histories (Guignard & Toplis, 2015; Trieloff et al., 2003). However, a number of samples have cooling rates inconsistent with the onion shell model. This discrepancy has been used to support rubble pile models (Ganguly et al., 2013, 2016; Kessel et al., 2007; Lucas et al., 2020; Ream, 2019; Scott et al., 2014; Taylor et al., 1987).

Attempts have been made to reconcile these seemingly contradictory observations in the framework of both the onion shell and rubble pile models. Given an onion shell model, it has been argued that impacts could excavate some material while leaving the rest of the onion shell structure intact. In this scenario, the excavated materials would record faster cooling rates than those predicted by the onion shell model and non-excavated material would continue to cool at an unaltered onion shell-consistent rate (Archer et al., 2019; Harrison & Grimm, 2010; Hellmann et al., 2019; Telus et al., 2014). Alternatively, it has been proposed that a large impact into a young, hot, and ductile H parent body could have resulted in uplift at the impact site, disturbing the uplifted materials from expected onion shell cooling rates (Ciesla et al., 2013). In the case of the rubble pile model, it has been argued that some thermochronologic systems (such as Pb–Pb dating) record the cooling rates prior to the disruption event whereas others (such as metallographic diffusion of Ni) record the cooling rates of the postimpact reaccreted parent body (Blackburn et al., 2017; Ganguly et al., 2013; Lucas et al., 2020).

To further investigate the thermal and impact histories of the H4 chondrite samples, we employ a microstructural approach to complement the existing cooling rate data of H4 chondrites. By using electron backscatter diffraction (EBSD) to examine dislocation activity in sample olivine, we can infer the temperature regime at which deformation occurred (Goudy, 2019; Hugo et al., 2019; Ruzicka & Hugo, 2018). By the same olivine dislocation observations, we can also assess postdeformational annealing, which imposes additional temperature constraints on the sample following its deformation (Goudy, 2019; Hugo et al., 2019; Ruzicka & Hugo, 2018). Through this approach, we can infer if each of our samples was impact-shocked, at what temperature regime that shock occurred, and if they remained buried to cool slowly at depth or were excavated to cool quickly on or near the surface of their parent body.

SAMPLES AND METHODS

Samples

Our H4 samples represent a spread of inferred cooling histories, with three fast cooled samples (Beaver Creek, Forest Vale, and Ste. Marguerite) and two slow-cooled samples (Quenggouk and Sena), with the slow-cooled ones having been interpreted to have cooled at depth and the fast-cooled ones to have been excavated by impacts. This is supported by studies on metallographic cooling rate measurement, evidence of live ^{26}Al at time of plagioclase closure, two pyroxene and spinel–olivine geothermometers, and both Pb–Pb and Ar-Ar dating (Ganguly et al., 2013; Scott et al., 2014; Taylor et al., 1987; Telus et al., 2014; Trieloff et al., 2003). All of these samples have low assessed shock stages of S1-S2 (Rubin, 2004; Scott et al., 2014; Stöffler et al., 1992), though one study found a shock stage of S3 for Beaver Creek (Rubin, 1994) in discordance with two others that find a shock stage of S1 for it (Scott et al., 2014; Stöffler et al., 1992).

EBSD Analyses

Electron backscatter diffraction is a scanning electron microscope (SEM) technique that maps crystallographic orientations and mineral identities by diffracting an electron beam through a mineral and processing the resultant diffraction patterns (Prior et al., 1999). Dislocation systems within olivine grains that are responsible for their deformation can be inferred from the difference in orientation between neighboring EBSD-mapped pixels, due to a geometric relationship between the crystallographic rotation axis (CRA) describing that orientation difference and the slip direction of the dislocation system (Lloyd et al., 1997). The particular dislocation system accommodating olivine deformation is strongly temperature dependent, with a-slip dislocation systems preferentially active at higher temperatures (roughly >800°C) than c-slip systems, allowing EBSD to be used to infer temperature of olivine grains during a past deformation event (e.g., de Kloe et al., 2002; Karato et al., 2008). Furthermore, EBSD can also be used to infer annealing in deformed olivine grains, as the process clears some grains of dislocations while in others preserving them within subgrain boundaries (Ashworth, 1981). This results in a skewed distribution of overall olivine grain deformation, measurable as GOS with EBSD, which can serve as an indicator of annealing (Ruzicka & Hugo, 2018). Both of these techniques have been successfully applied in ordinary chondrites within the past few years, providing a body of reference data to help interpret the deformational, thermal, and annealing

histories of ordinary chondrites (Goudy, 2019; Hugo et al., 2019; Ruzicka & Hugo, 2018).

The EBSD methods in this study follow those of Ruzicka and Hugo (2018). Thin section H4 samples were additionally hand polished with colloidal silica for 75 min and covered with 5 nm carbon coats. EBSD data were collected using the Oxford Symmetry detector on a Thermoscientific Apreo field emission SEM equipped with Aztec software, using step sizes of 2 or 4 μm, a beam current of 10 nA, and an accelerating voltage of 20 kV. Mapped sections were quadrilateral polygons designed to maximize the captured surface area of each sample thin section without intersecting the perimeters of the samples.

EBSD Data Analyses

After collection, the EBSD data were exported from Aztec to be processed in Channel 5 software (version 5.12.73.0). In Channel 5, grains were mapped with a minimum grain size of five contiguous pixels and a critical misorientation of 15°. GOS values for the resulting olivine grains were calculated by the software. Also using Channel 5, olivine CRA data from interpixel crystallographic misorientations of 2°–10° were processed and plotted in crystallographic stereonets, with a contour half width of 25°. CRA pole densities at the crystallographic poles of the stereonets were measured and used to calculate the fraction of CRA poles associated with a-slip for each map. Processed grain data were exported from Channel 5 as Excel files and processed with a custom R script to calculate the skew in GOS populations of all olivine grains of ≥50 μm diameter.

In our statistics, we propagate uncertainties by conventional means. This is to say, that if two values are added or subtracted, such as in "$c = a \pm b$," then $\sigma_c = (\sigma_a{}^2 + \sigma_b{}^2)^{0.5}$, with σ being the variable for the error or standard deviation. And if two values are multiplied or divided, such as in "$c = a \times b$" or "$c = a \div b$," then $\sigma_c = c \times [(\sigma_a \div a)^2 + (\sigma_b \div b)^2]^{0.5}$. Standard errors of sample means and medians are also calculated conventionally, as $\sigma_{Mean} = \sigma_{Sample} \div (n_{Sample} - 1)^{0.5}$ and $\sigma_{Median} = (\pi \div 2)^{0.5} \times \sigma_{Sample} \div (n_{Sample} - 1)^{0.5}$, with n being the number of observations in the sample. As follows from these conventions for standard errors of means and medians and the principles of error propagation, we calculate the error on our skew (mean/median) values by the following:

$$\sigma_{Skew} = \frac{\sigma_{sample}}{Median^2} \times \sqrt{\frac{(\pi \times Mean^2) + (2 \times Median^2)}{2 \times (n_{sample} - 1)}}$$

A natural consequence of this calculation is that the error of a skew value increases proportionally with the value of the skew itself. As the standard errors of means, medians, and skewness values are all normally distributed, we calculate a range of 95% error for any of them to be $1.96 \times \sigma$.

We can constrain the temperature regime of shock metamorphism from the fraction of a-slip system CRA poles ($f_{<010>} + f_{<001>}$; de Kloe et al., 2002; Ruzicka & Hugo, 2018). For calculating the statistics of the CRA-based temperature parameter, we treated our data set as a collection of binary values. The value of CRA poles corresponding to a-slip dislocation systems was 1, and the value of CRA poles corresponding to the c-slip system was 0, with poles considered to be corresponding to a slip system if they are within 25° of the ideal CRA of that slip system. While for our methods we assume that <010> results primarily from a-slip systems, it is possible for them to be created by c-slip screw systems, but this is unlikely (Karato et al., 2008). Since the temperature parameter is the fraction of system-related CRA poles related to a-slip systems, the mean of this data population is the same temperature parameter that is calculated using 25° half-width pole densities. While the temperature parameter calculation that uses pole densities does not require precise information on the number of CRA poles within 25° of the ideal CRAs of the slip systems, that information is necessary to determine the standard deviation of the aforementioned binaric population. Unfortunately, the exact orientation data of the CRA poles cannot be extracted from the Aztec data files using the Channel 5 software.

To constrain the standard deviation of the binaric population for the temperature parameter, we make an intentional underestimation of the pole numbers associated with the slip systems of olivine. Recognizing that while not all observed CRA poles plot close enough to an ideal slip system CRA to be counted with one, we chose to assume that only ~9.4% of measured poles plot sufficiently near the ideal CRA poles of the system to be considered corresponding to those poles. This is because the areal fraction of the crystallographic stereonet that is sufficiently close to the one of the ideal CRA poles to be correspondent with them is ~9.4% of the total area of the stereonet (precisely, the fraction is [1 – cos 25°]). If the number of poles within the correspondence area of the ideal CRA poles were less than this fraction, then it should be observed that the highest point of pole density should be outside the correspondence area of all ideal CRA slip-system poles, and this is not the case for any of the samples. Therefore, the most conservative size of the real binaric statistical population is ~9.4% of the measured CRA poles for each sample. The real population size is likely larger than this minimum value, so it serves as the maximum assumed population size that can be trusted to equal or underestimate it, and thereby provide the smallest

reliable overestimation of the population's standard deviation.

With the binaric population conservatively underestimated, and the proportion of a-slip and c-slip corresponding poles known, the correct number of 1 and 0 values is assigned to fill out the population, and its standard deviation and standard error of its mean are calculated. Since its mean is the temperature parameter, the standard error of the mean is the error of the temperature parameter. Furthermore, due to the central limit theorem, the probability distribution of the temperature parameter must be normally distributed, due to it being the mean of sample population.

Petrographic Analyses

Quenggouk, Sena, and Ste. Marguerite were further examined for proposed petrographic indicators of shock that could survive annealing (Rubin, 1994, 2004). This consisted of creating EDS mosaics using the aforementioned SEM at a current of 1.0 nA, accelerating voltage of 15 kV, and a pixel size of 1.6 μm. These EDS maps were used with the 4 μm step size EBSD maps of the meteorites to examine the following two petrographic shock indicators: irregularly shaped troilite grains within Fe metal grains and metallic Cu grains (Rubin, 1994, 2004). The presence or absence of these features was used to infer a probable pre-annealing shock stage, provided any such evidence was found.

RESULTS

EBSD Grain Deformation Signatures

Inferred annealing (GOS skew) and temperature parameters ($f_{<010>} + f_{<001>}$) for the collected EBSD maps are shown in Table 1. These data are graphed in Figure 1 and compared to reference data for differing interpreted histories of codeformational temperature and annealing. Example subregions of the EBSD maps of Forest Vale and Quenggouk are shown in Figures 2 and 3. Figure 4 displays equally sized subsections from the centers of EBSD GOS maps for all samples as well as two reference samples, Kernouvé (Ruzicka & Hugo, 2018) and Tieschitz (Goudy, 2019). Figure 5 displays CRA stereonets for all sample meteorites. Figure 6 displays the GOS standard deviation values of our samples alongside those of reference samples from the literature (Goudy, 2019; Hugo et al., 2019; Ruzicka et al., 2020; Ruzicka & Hugo, 2018). Grain reference orientation deviation (GROD) maps for the olivine grains of the samples are provided in the online supplement, all on a 0°–20° color scale. GROD maps show the orientational deviation of measured pixels with the grains from a reference pixel within each grain. Subgrain boundaries are visible as regions of sharp color change within grains.

GOS skew, calculated as mean olivine GOS of a sample divided by the median olivine GOS, can be an indicator of recovery (annealing of dislocations) in the olivine grains (Ruzicka & Hugo, 2018), as stated in the previous section. The parameter $f_{<010>} + f_{<001>}$ measures the fraction of observed CRA pole densities associated with the high-temperature a-slip dislocation systems of olivine. Although it is possible for c-slip systems to result in <010> CRA poles; regardless, higher values of this parameter are associated with higher codeformational temperature conditions (Ruzicka & Hugo, 2018). To provide context, our sample data in these parameters are graphed in Figure 1 alongside regions defined by data from previous studies of meteorites interpreted to have a variety of temperature conditions during shock metamorphism ($f_{<010>} + f_{<001>}$ parameter) and postshock annealing (GOS skew). These histories are shock metamorphism after the end of thermal metamorphism without annealing ("Cold Shocked"; Bruderheim, Elbert, Leedey, and Morrow County; Hugo et al., 2019; Ruzicka & Hugo, 2018; Ruzicka et al., 2015), shock metamorphism during the period of thermal metamorphism without annealing ("Hot Shocked"; Saint-Séverin; Hugo et al., 2019), and shock metamorphism concurrent with thermal metamorphism with subsequent annealing ("Hot Shocked and Annealed"; Kernouvé, MIL 99301 host rock, Portales Valley; Ruzicka et al., 2015; Ruzicka & Hugo, 2018). No regions or clasts of anomalously elevated GOS similar to the clast observed within MIL 99301 by Ruzicka and Hugo (2018) were observed in our samples.

The H4 chondrites in this study have broadly similar data and are best consistent with reference samples interpreted to have been impact-shocked while metamorphically hot with subsequent postshock annealing, as can be seen in Figure 1. Beaver Creek and Quenggouk have similar data in both GOS skewness (mean GOS/median GOS) and $f_{<010>} + f_{<001>}$, with values of 1.50 ± 0.13 and 1.56 ± 0.20 for the former parameter and 0.692 ± 0.003 and 0.706 ± 0.003 for the latter. Forest Vale has an $f_{<010>} + f_{<001>}$ parameter of 0.698 ± 0.003, subequal to that of Beaver Creek and Quenggouk, but a GOS skew of 2.32 ± 0.43, significantly higher than those two meteorites. Forest Vale plots closest to the reference region of hot shocked and annealed sample data. Sainte Marguerite has an $f_{<010>} + f_{<001>}$ parameter of 0.765 ± 0.002, higher than any other sample in this study. Like Forest Vale, it has an exceptionally high GOS skew of 2.06 ± 0.36 and plots above the region for annealed samples (Figure 1). The two EBSD maps of the same Sena thin section have similar data and cover overlapping, but slightly different areas, at different recorded step sizes (one at 2 μm and the other at 4 μm). Both Sena data sets have

TABLE 1. Electron backscatter diffraction (EBSD) annealing and temperature parameters.[a]

Sample (step size in μm)	Mean GOS (1 SD)	Mean GOS/ median GOS	Grains >50 μm	$f_{<010>} + f_{<001>}$	CRA poles	Shock stage	Area (mm^2)
Beaver Creek (4)	1.48 (1.33)	1.50 ± 0.18	1397	0.706 ± 0.008	129,961	S1[c,f], S3[d]	84.98
Forest Vale (2)	1.56 (1.92)	2.32 ± 0.34	1391	0.698 ± 0.008	131,976	S1[f], S2[e]	74.85
Quenggouk (2)	2.11 (2.08)	1.56 ± 0.26	936	0.695 ± 0.005	293,111	S2[c]	49.20
Sena (4)[b]	0.69 (0.96)	1.83 ± 0.38	1541	0.588 ± 0.025	15,150	S1[f]	96.42
Sena (2)[b]	0.68 (1.11)	2.26 ± 0.27	1236	0.579 ± 0.014	47,157	S1[f]	68.64
Ste. Marguerite (2)	1.82 (2.06)	2.06 ± 0.49	1018	0.765 ± 0.006	164,689	S2[e]	52.48

Note: Elevated GOS skew (roughly >1.25) is an indicator of annealing. Elevated $f_{<010>} + f_{<001>}$ (roughly >0.5) indicates olivine deformation is primarily accommodated by slip systems active at >800°C, given that the effects of grain orientation relative to the deviatoric stresses are ignored. Mean and median GOS are calculated for the population of grains greater than 50 μm in diameter.
Abbreviations: CRA, crystallographic rotation axes; GOS, grain orientation spread.
[a]Ranges are 95% propagated standard errors. Reference for parameters: Ruzicka and Hugo (2018).
[b]Two maps of the same Sena sample were collected at different step sizes.
[c]Stöffler et al. (1992).
[d]Rubin (1994).
[e]Rubin (2004).
[f]Scott et al. (2014).

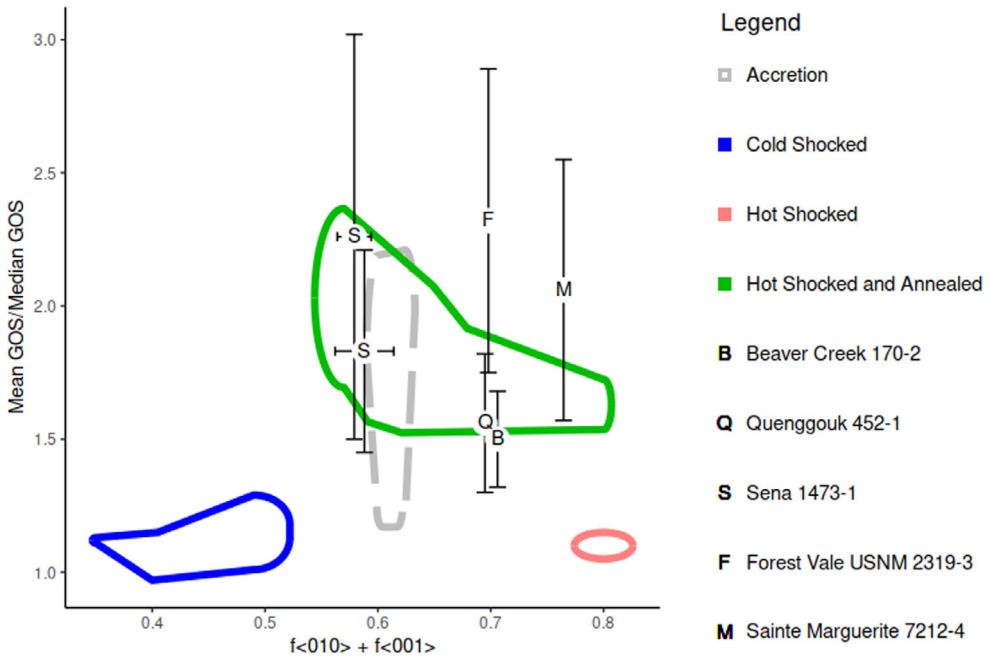

FIGURE 1. Inferred annealing (Mean GOS/Median GOS) and deformational temperature ($f_{<010>} + f_{<001>}$) plot. Dashed gray perimeter is the reference region for accretion-related deformation in type 3 ordinary chondrites (Goudy, 2019; Ruzicka et al., 2020). Green perimeter is reference data region for samples shocked while hot and subsequently annealed (Ruzicka & Hugo, 2018). Blue perimeter is reference data region for samples shocked while cold and not annealed (Hugo et al., 2019; Ruzicka & Hugo, 2018). Red perimeter is reference data region for a sample that was shocked while hot and not annealed (Hugo et al., 2019). B is Beaver Creek, F is Forest Vale, M is Ste. Marguerite, Q is Quenggouk, and S is Sena. Mean GOS/Median GOS (grain orientation spread) is the inferred annealing parameter, and $f_{<010>} + f_{<001>}$ is the inferred deformational temperature parameter (Ruzicka & Hugo, 2018). Error bars are 2σ, and *x*-axis error bars are smaller than the size of the symbols they describe in most cases. (Color figure can be viewed at wileyonlinelibrary.com.)

notably lower $f_{<010>} + f_{<001>}$ parameters, 0.588 ± 0.009 (4 μm map) and 0.579 ± 0.005 (2 μm map), than the other studied meteorites. The 4 μm step size Sena map has a GOS skew of 1.83 ± 0.21, which is moderate compared to the other samples and plots into the reference region for annealed meteorites. The 2 μm step size Sena map has an elevated GOS skew, 2.26 ± 0.42, like those of Forest Vale and Sainte Marguerite.

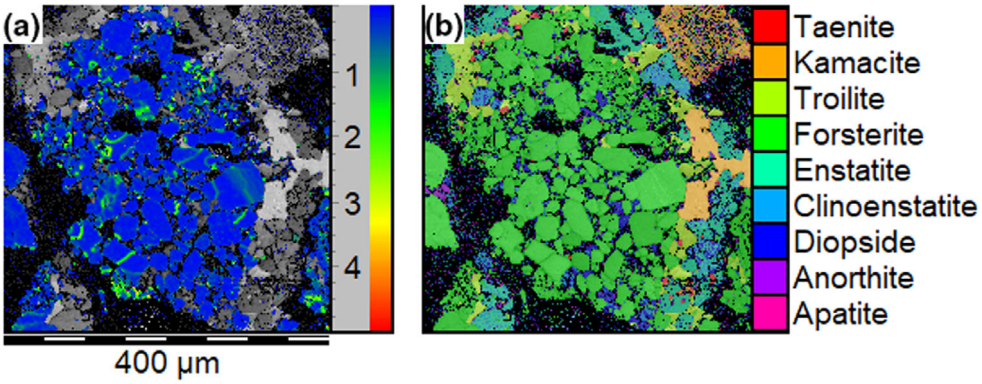

FIGURE 2. Small electron backscatter diffraction (EBSD) map region of Forest Vale. a) Local misorientation map section of olivine grains in units of degrees. Local misorientation is measured by a kernel function calculating the misorientation within the kernel area immediately surrounding a pixel. Regions of elevated misorientation within a grain are probable subgrain boundaries. b) Phase map section of the same region. Identified phases reflect mineral structure, not composition: forsterite represents all olivine, enstatite all orthopyroxene, etc. Both map sections have an underlying grayscale band contrast layer in addition to their phase or local misorientation layers. (Color figure can be viewed at wileyonlinelibrary.com.)

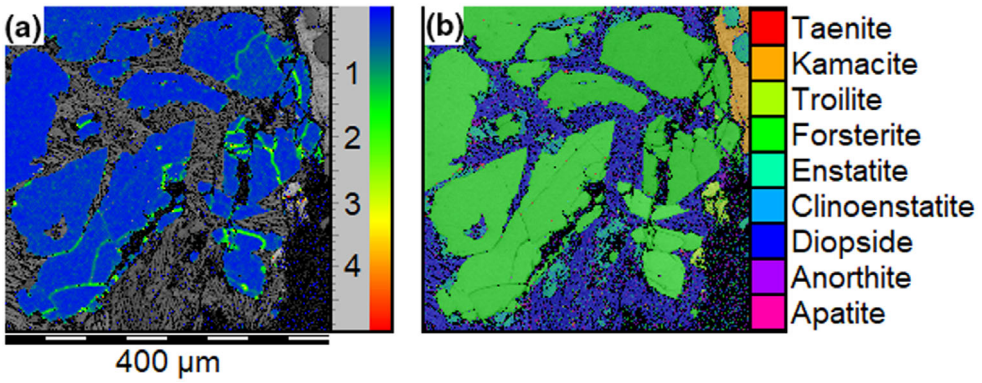

FIGURE 3. Small electron backscatter diffraction (EBSD) map region of Quenggouk. a) Local misorientation map section of olivine grains in units of degrees. Local misorientation is measured by a kernel function calculating the misorientation within the kernel area immediately surrounding a pixel. Regions of elevated misorientation within a grain are probable subgrain boundaries. b) Phase map section of the same region. Identified phases reflect mineral structure, not composition: forsterite represents all olivine, enstatite all orthopyroxene, etc. Both map sections have an underlying grayscale band contrast layer in addition to their phase or local misorientation layers. (Color figure can be viewed at wileyonlinelibrary.com.)

Petrographic Observations

Proposed petrographic shock indicators such as irregular troilite grains within Fe metal and metallic Cu grains were observed in Sena at an occurrence abundance of 8.8 (number of occurrences per $mm^2 \times 100$, as defined by Rubin, 1994), while other petrographic shock features described by Rubin (2004) were not observed. Metallic copper was observed in Quenggouk at an occurrence abundance of 3.3, alongside occurrences of irregular troilite grains within Fe metal. In Ste. Marguerite, no textures of irregular troilite within Fe metal were found, but the sample has a metallic Cu occurrence abundance of 7.5. The observed occurrence abundances of metallic copper in all examined samples are higher than the proposed threshold of 2.5 required to indicate shock (Rubin, 1994).

DISCUSSION

H Chondrite Parent Body Models

Two primary types of models for the first 100 Ma history of the H parent body have dominated discussion in recent decades. In the first of these, the onion models, the H parent body is composed of concentric shells of increasing metamorphic grade, with type 3 material at the surface and type 6 in the center, with higher grade material experiencing higher peak temperatures and/or longer durations of metamorphism (e.g., Monnereau et al., 2013).

H chondrites displaying an inverse correlation between metamorphic grade and cooling rate have been used to support this view (Guignard & Toplis, 2015; Trieloff et al., 2003). In the second view, this onion shell structure is disrupted and scrambled by a large impact during the time period of metamorphism, perturbing the neat relationship between metamorphic grade and cooling rates expected under the onion shell model. A number of H chondrites found to have such inconsistencies in metamorphic grade and cooling rates have been used to argue for this second model (Ganguly et al., 2013, 2016; Kessel et al., 2007; Lucas et al., 2020; Ream, 2019; Scott et al., 2014; Taylor et al., 1987).

Both cases have thus far been founded empirically in two types of geochemical technique. The first of these are diffusion-based techniques that can reveal cooling rates at specific temperature ranges, such kamacite–taenite Ni diffusion (i.e., Scott et al., 2014). The second of these are radiogenic dating approaches, such as Pb–Pb dating and Ar-Ar dating (i.e., Trieloff et al., 2003). These are used in two ways. Firstly, two long-lived systems with different closure temperatures can be used to date the two points in time when a chondrite cooled through each of those closure temperatures, and a cooling rate is calculated from the differences in those times and the values of the two closure temperatures (Trieloff et al., 2003). Secondly, one can look for evidence of short-lived systems such as ^{26}Al-^{26}Mg still being active at the time of a chondrite's cooling, as was done by Telus et al. (2014). If such evidence is found, then the time that the sample cooled through the closure temperature of that system can be determined. If not, then that observation indicates that the sample was above that closure temperature for the lifespan of that short-lived system.

Constraints from EBSD Deformation Signatures

Our olivine-targeting EBSD technique adds an entirely new form of information to previous techniques: (1) the temperature regime at which a sample was deformed and (2) whether that sample remained at high temperature following that deformation for long enough that annealing could occur. This technique can tell us whether a sample has been shocked or not, even if conventional indications of shock used by the classification system of Stöffler et al. (1991, 2018) have been removed by annealing (Goudy, 2019; Hugo et al., 2019; Ruzicka & Hugo, 2018). We can infer whether a sample was shocked while hotter than or cooler than about 800°C (Goudy, 2019; Hugo et al., 2019; Ruzicka & Hugo, 2018). These techniques can tell us whether after being shocked, the sample remained hot enough (~>600°C) for long enough for its olivine grains to anneal, which would be indicated by a high grain orientation spread (GOS) skewness (Goudy, 2019; Hugo et al., 2019; Ruzicka & Hugo, 2018). If our samples experienced any shock metamorphism from an impact, these inferences should enable us to determine whether that shock happened while the parent body was undergoing thermal metamorphism, and in the case that the body was, whether those samples were excavated to cool quickly at or near the surface, or left buried to cool slowly.

From existing research on our samples, we can make predictions about what we should find with the EBSD techniques. That literature indicates rapid cooling ($\geq$5000 K Myr^{-1}) for Beaver Creek, Forest Vale, and Ste. Marguerite, which should not allow time for annealing (Ganguly et al., 2013; Scott et al., 2014; Taylor et al., 1987; Telus et al., 2014; Trieloff et al., 2003), these samples should plot in the "hot shocked" region of Figure 1, in concordance with reference data (Ruzicka & Hugo, 2018) for samples that were shocked while metamorphically hot and which cooled quickly without chance for annealing. Conversely, Quenggouk and Sena should, if shocked after thermal metamorphism, plot alongside cold shocked samples, or if shocked during metamorphism, plot with hot shocked and annealed reference data (Hugo et al., 2019; Ruzicka & Hugo, 2018), due to their slow cooling rates found by past studies (Scott et al., 2014; Taylor et al., 1987; Telus et al., 2014; Trieloff et al., 2003). This allows the exclusion of an expected history of hot shock without annealing, as that would require rapid cooling to prevent annealing. Quenggouk and Sena fall within these expectations; both have parameters consistent with reference data for hot shocked and annealed samples. This is also consistent with transmission electron microscopy (TEM) observations by past workers on Quenggouk, who found evidence for annealed deformation in the olivine by way of dislocation recovery (Ashworth, 1981). However, Beaver Creek, Forest Vale, and Ste. Marguerite also plot within the same field. Like Quenggouk, this is consistent with previous TEM analyses of Beaver Creek (Ashworth, 1981) and the presence of petrographic shock features in Ste. Marguerite consistent with shock stages of S3+, higher than its current one of S2 (Rubin, 2004). Furthermore, distinct subgrains within larger olivine grains can be seen in the GROD maps of our samples (located in the online supplement), showing subgrain formation consistent with annealing processes. These observations suggest that a history of synmetamorphic shock and postshock annealing can be inferred for all samples in this study.

Shock Metamorphism Versus Accretional Deformation

In contrast to grain deformation from shock metamorphism (deformation resulting from impact processes), accretional deformation is grain deformation

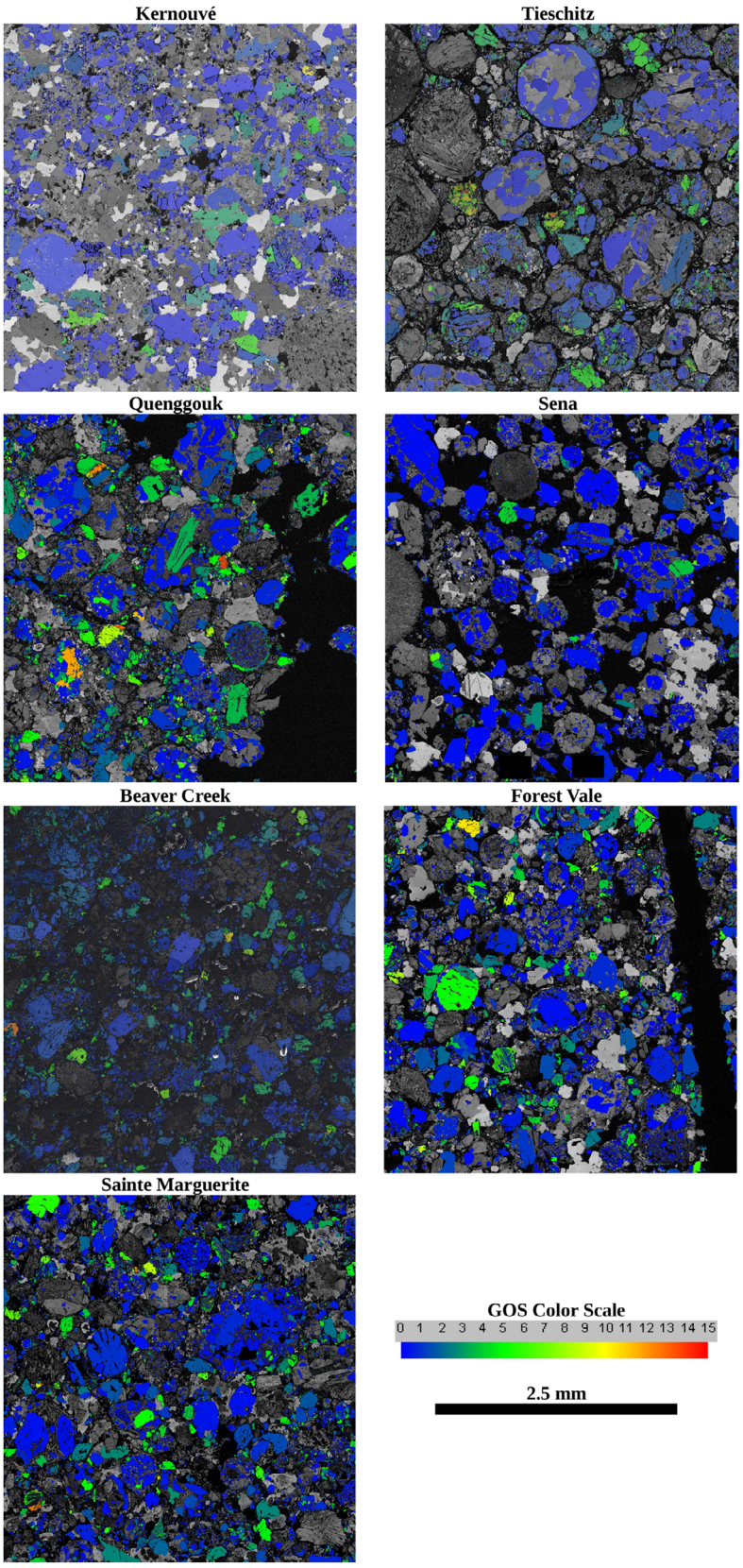

FIGURE 4. Comparative grain orientation spread (GOS) maps. Shown sections are ~3790 μm square map sections from the center of electron backscatter diffraction (EBSD) large area maps of our samples and Kernouvé (Ruzicka & Hugo, 2018) and Tieschitz (Goudy, 2019). Kernouvé is an example of an H6 chondrite subject to synmetamorphic impact shock and postshock annealing (Ruzicka & Hugo, 2018). Tieschitz is an example of an H/L3 chondrite preserving the deformation of hot chondrule accretion (Goudy, 2019). These two-type examples can be qualitatively distinguished by the scale of deformational variability, with shock-related deformation variability occurring on a grain size scale and with accretional deformation variability occurring on a chondrule size scale; in Tieschitz, grains within the same chondrules have similar GOS values, whereas this is not true of Kernouvé. The map sections of our samples have deformation on the grain size scale, consistent with Kernouvé and shock deformation, and inconsistent with Tieschitz and accretional deformation. Map section of Sena shown is from the 2 μm step-size EBSD map. Size of map sections was chosen to balance maximization of area displayed with retention of discernible detail. All map sections have an underlying grayscale band contrast layer in addition to their GOS value layers. (Color figure can be viewed at wileyonlinelibrary.com.)

resulting from the process of chondrite parent body formation wherein chondrules, dust, and other materials accrete from the solar nebula into or onto a parent body. The concept of accretional deformation is primarily argued for on the basis of textural observations such as mutual deformation between chondrules and surrounding objects, close-fit cluster chondrite textures, and in one case, a "burst" chondrule (i.e., Hutchison, 1996; Metzler, 2012), but the research existing on the topic is scarce, and so requires further work to validate or refute. Previously studied type 3 S1 ordinary chondrites with accretion-associated deformation signatures, a "squashing" of chondrules and their mineral grains, characterized by cluster chondrite textures (~90 vol% chondrules; Metzler, 2012), fall into a wide range of GOS skews, but only a narrow range of $f_{<010>} + f_{<001>}$ parameters: 0.592–0.640 (Goudy, 2019). Notably, Sena has an $f_{<010>} + f_{<001>}$ parameter of 0.585, which potentially indicates accretional deformation as a source for its observed deformation rather than shock metamorphism.

Given that the deformation history of Sena is indeterminate from its EBSD parameter data alone, we investigated proposed petrographic shock features following a study by Rubin (2004), which examined 210 type 4–6 ordinary chondrites for 12 proposed shock textures associated with shock degrees of S3+ levels that can survive annealing to S1-S2 levels. Looking for these same features, we found that Sena contains two such petrographic shock features, elevated occurrence of metallic copper and irregular troilite grains within Fe metal, consistent with shock metamorphism of S3-S6 (Rubin, 1994, 2004) that cannot be readily credited to accretional deformation. Given an absence of features associated with shock stages higher than S3 (Rubin, 2004), a possible pre-annealing shock stage of S3 can be tentatively suggested for Sena, if the proposed shock features are accurate. On the basis of those observations, shock metamorphism is favorable over accretion as the cause of the $f_{<010>} + f_{<001>}$ parameter value and as the source of the pre-recovery olivine deformation.

We also evaluated the scale of deformational variability, which is the scale on which the deformation occurs. In accretional deformation, deformation occurs on the chondrule scale, with the individual chondrules deforming as whole objects, due to their differing susceptibilities to deformation upon accretion (Goudy, 2019). These differing susceptibilities are likely due to their differences in temperature at accretion and their composition, with chondrules being more deformable the hotter and more ferroan they are. Thus, the olivine grains of individual chondrules display similar GOS values, as they have deformed together during the accretion of their chondrules. In shock-related deformation, the deformation instead occurs on the scale of the individual grains, with the result being that grains within the same chondrule can display a wide range of GOS values (Ruzicka & Hugo, 2018). Figure 4 shows GOS map sections of our samples and reference samples for accretional and shock-related deformation. This comparison indicates that our samples have deformation on the grain size scale, which is consistent with Kernouvé-like shock deformation, and inconsistent with Tieschitz-like accretional deformation.

Another possible indicator of accretional deformation is the observed GOS standard deviation in the sample's olivine grains (Ruzicka et al., 2020). As can be seen in Figure 6, meteorites with histories of postshock annealing, unannealed shock metamorphism, and accretional deformation all fall within distinct ranges of GOS standard deviation. While two of our samples, Beaver Creek and Sena, have data consistent with postshock annealing, our other three samples, Forest Vale, Quenggouk, and Ste. Marguerite, have data more consistent with accretional deformation, and inconsistent with shock processes, annealed or not. This is despite their scale of deformation and $f_{<010>} + f_{<001>}$ parameters being consistent with shock processes and inconsistent with accretional deformation. It is intuitive that there might be a relationship between GOS SD and GOS skew, as during annealing, GOS is lowered in most grains but preserved unaltered in others by subgrain boundary formation. This would suggest that GOS SD and GOS skew should be

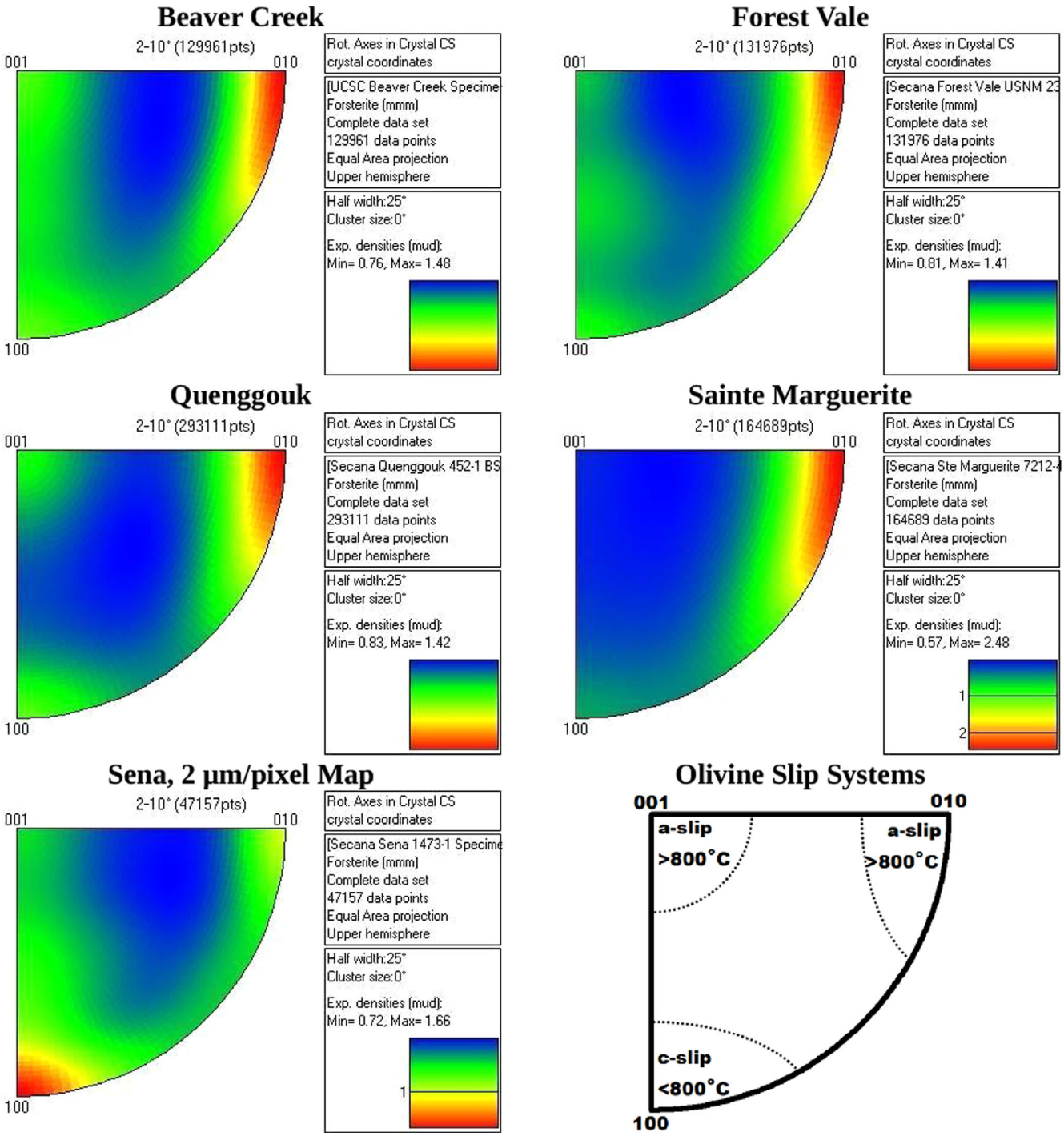

FIGURE 5. Crystallographic rotation axes (CRA) stereonets of electron backscatter diffraction (EBSD) maps. Color scales for the maps indicate local densities of olivine CRA poles determined by a kernel function for an interpixel misorientation range of 2°–10°. Simplified guide for interpretation of olivine slip system Burgers vectors and approximate favored temperature regimes from CRA regions is present in the lower right, including approximate 25° half-width areas associated with the poles (de Kloe et al., 2002; Ruzicka & Hugo, 2018). The $f_{<010>} + f_{<001>}$ parameter used to infer codeformational temperature conditions is the fraction of the pole densities located in the "corners" associated with the high temperature a-slip olivine dislocation systems, out of the sum of the pole densities in all three "corners" which each encompass one of the three primary dislocation systems of olivine, two of which are for a-slip systems. This is why despite appearances, in the Sena CRA stereonet high temperature a-slip activities collectively outweigh the c-slip activities, as the two a-slip corners (32.6% and 25.3% of activities) add up to 57.9% of the dislocation system activities, compared to the 42.1% for c-slip. (Color figure can be viewed at wileyonlinelibrary.com.)

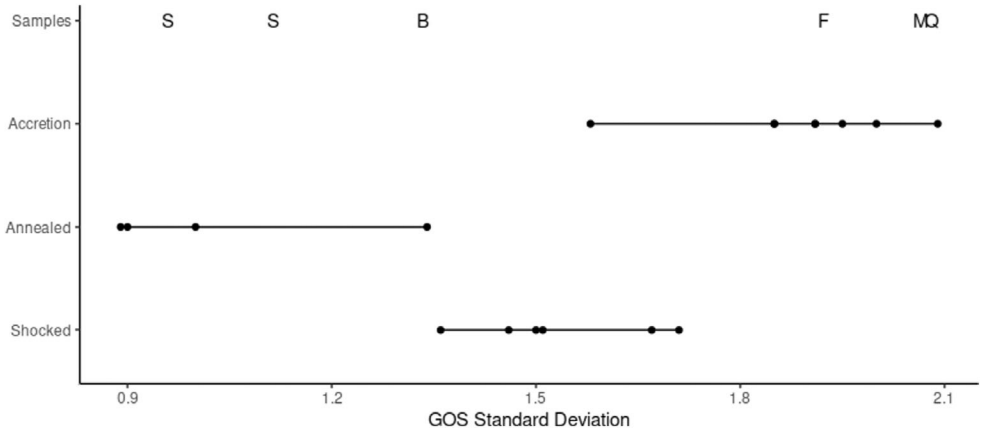

FIGURE 6. Comparative chart of grain orientation spread (GOS) standard deviation. Figure shows the GOS population standard deviations for our sample population compared to reference data for values associated with accretional deformation, postshock annealing, and unannealed shock metamorphism. Our data for Sena and Beaver Creek are consistent with the reference data for postshock annealing, and our data for Forest Vale, Quenggouk, and Ste. Marguerite are consistent with accretional deformation. "B" is Beaver Creek, "F" is Forest Vale, "M" is Ste. Marguerite, "Q" is Quenggouk, and "S" is Sena. Reference data are from Goudy (2019), Hugo et al. (2019), Ruzicka and Hugo (2018), and Ruzicka et al. (2020).

correlated. A linear model comparing GOS SD (y variable) and GOS skew (x variable) data for our samples produces a slope of 0.019 ± 0.179 degrees (1σ error), which is statistically indistinguishable from a slope of zero. Thus, there is no discernible correlation between the two metrics, supporting that GOS SD can serve as an independent indicator of deformation in olivine grains.

An alternative explanation for the chondrule deformation viewed in these samples would be nebular collisions between chondrules rendered ductile by the heating of the chondrule-forming process, which could cool in distorted shapes and then accrete at a lower non-ductile temperature state. The close-fit textures of the samples in the aforementioned works (Goudy, 2019; Ruzicka et al., 2020) imply mutual codeformation of chondrules of differing ductilities, with chondrite matrix material trapped in-between, which renders in situ deformation more favorable as an interpretation than collisions within the solar nebula. As is visible in the GROD maps of our online supplement, these same mutual deformation cluster chondrite textures can also be found in all of our samples, and so by the same reasoning, in situ deformation of ductile chondrules is a preferred explanation for the texture with the attendant implications of the aforementioned studies. Therefore, while some caution cannot be forgotten, we consider the possibility of accretion to be one that requires serious consideration in our interpretations.

There is another issue that must be considered. The presence of highly deformed clasts incorporated into our meteorite samples could potentially cause elevated GOS skewness values beyond accretional deformation, which would conflict with an interpretation of synmetamorphic shock with postshock annealing, similar to the high-deformation clast observed in MIL 99301 by Ruzicka and Hugo (2018). If this were the case for any of our samples, such a clast should be observable within our GOS maps, but no such clast has been found. Instead, the vast majority of olivine grains have low GOS values, with a qualitatively even and unconcentrated distribution of higher GOS grains spread across the mapped areas, as can be seen in Figure 4. Such homogeneous spatial distribution of low and elevated GOS grains is what would be expected of a history of distributed deformation followed by annealing (Ruzicka & Hugo, 2018).

Evidence for Multiple Early Impacts

Taking into account the existing literature for these samples alongside with the general, although not total, consistency of our data and observations with shock processes and postshock annealing, we have interpreted the following histories for our samples. Quenggouk and Sena were affected by an impact but without excavation. Left at depth, annealing could occur in their olivine grains. This is similar to the inferred histories of some other H chondrites: Butsura (H6), Kernouvé (H6), and Portales Valley (H6) (Friedrich et al., 2017; Ruzicka & Hugo, 2018; Ruzicka et al., 2015). The fast-cooled samples Beaver Creek, Forest Vale, and Ste. Marguerite also have this same history, but after annealing, they were excavated by subsequent impact(s) to cool quickly on the surface. These fast-cooled samples have each experienced at least two impacts prior to ~6 Ma post-CAI formation.

However, the existence of signatures of accretional deformation in Forest Vale, Quenggouk, and Ste.

Marguerite, and the possible signatures of the same in Sena, coexisting with signs of shock processes, complicate this simplistic picture. We take the most straightforward approach to resolving this conflict: We interpret that most of the samples retain traces of the accretional deformation of their chondrules, which has been overprinted by later processes of impact shock and annealing. These accretional signals survive in these samples because they have not been sufficiently metamorphosed to remove it at their low type 4 grade of metamorphism, having not reached a high enough temperature and/or not having been hot for long enough to anneal those signals, depending on which model of chondrite metamorphism is correct. Our samples may further indicate that the coexistence of shock and accretional signatures may be typical of type 4 chondrites, though since one or two of our samples are without lingering evidence of accretional deformation, Sena and Beaver Creek, it is possible that type 4 metamorphism can remove that evidence. Assuming that the accretional signature is removed by metamorphism, then it may be possible to use the presence or absence of these accretional signatures to infer a less metamorphosed subcategory of type 4 chondrites (those that display an accretional signal; "type 4.0") and a more metamorphosed subcategory of type 4 chondrites (those without an accretional signal; "type 4.5"). Further research would be required to verify this supposition.

The fast-cooled samples were excavated with live ^{26}Al, allowing for their times of excavation to be dated to about 5.2–6.5 Ma post-CAI formation (Telus et al., 2014; Zinner & Göpel, 2002). In the case of Ste. Marguerite, this timing is consistent with Pb–Pb dating implying rapid cooling for the meteorite (Bouvier et al., 2007). Assuming the first impact occurred at 2–3 Ma post-CAI formation, this allows for maximum annealing times of about 2.2–3.5 Myr. Is this time period for annealing sensible? While it is unclear what the average distance an olivine dislocation in these samples would have to travel to annihilate with another dislocation, aggregate into a subgrain boundary, or reach the edge of the crystal, reasonable conjectures can be made (Farla et al., 2011; Karato & Ogawa, 1982; Toriumi & Karato, 1978). The diffusion rate of dislocations is dependent on an activation energy, and accordingly the mobility of dislocations increases exponentially with temperature in accordance with an Arrhenius equation (Goetze & Kohlstedt, 1973). Using as a basis the recovery experiments of Ashworth and Mallinson (1985), in which it was observed that the naturally shocked L chondrite Kyushu could be annealed in 90 h at 1000°C, and the olivine dislocation diffusion equation of Goetze and Kohlstedt (1973), an average diffusion distance of 0.3 μm can be calculated. Utilizing this diffusion distance and the maximum annealing time allowed by ^{26}Al dating (Telus et al., 2014), a plausible minimum required annealing temperature of about 480°C can be calculated using the olivine dislocation diffusion equation of Goetze and Kohlstedt (1973), well below the expected temperatures of peak H4 metamorphism (e.g., Huss et al., 2006). So, a time period of 2.2–3.5 Myr is sensible for annealing in these samples.

The parent body history model that best fits our data and observations is that of an impact battered, but not disrupted, onion shell body at approximately 7 Ma after CAI formation. An undisturbed onion shell is incompatible with our inferred sample histories, as all have evidence consistent with one or more synmetamorphic impacts with the EBSD signatures of shocked and annealed samples (Figure 1). Reconciling a disrupted rubble pile model with our observations would require keeping Quenggouk and Sena (and other slow-cooled H4s) at elevated temperatures past the lifetime of the ^{26}Al-^{26}Mg system, since they did not cool below the closure temperature of this system while it was active. This may be achieved if these rocks do not cool too much while the H body is disrupted, or are sufficiently reheated following reassembly to reequilibrate the rocks, or if the disruption occurs after the system's lifetime has passed at about 7 Ma post-CAI formation, such as during the 30–70 Ma post-CAI formation timeframe proposed by Blackburn et al. (2017). If this latter option were the case, the excavation(s) evident in the fast-cooled samples would be unrelated to the parent body disruption event. Regardless, an early <7 Ma post-CAI formation disruption of the H chondrite parent body is difficult to reconcile with our inferred histories, implying instead an impact-battered intact onion shell for that time period.

The inferred histories of our samples, particularly those of Forest Vale and Ste. Marguerite, present an issue for previous studies that numerically modeled the thermal history of the H parent body. These studies employed both these meteorites as empirical anchors for their onion shell models (Henke et al., 2012; Monnereau et al., 2013). Use of these well-studied meteorites for this purpose requires that their thermal histories reflect that of an undisturbed onion shell. By the determination of this study, they do not. This conclusion is also supported by Lucas et al. (2020). Instead, these samples were excavated by impacts early in the history of their parent body and were left to cool on the surface at an accelerated rate. Using the thermal histories of these samples to model the onion shell thermal history of the H parent body is problematic. Future onion shell modeling work should not use these meteorites or any other fast-cooled H4 meteorites to avoid this issue. Slow-cooled H4s, such as the two in this study, Sena and Quenggouk, would be more appropriate.

This interpretation of EBSD data may be complicated by some new research, however. The existing parameter for indicating annealing, GOS skewness in the population

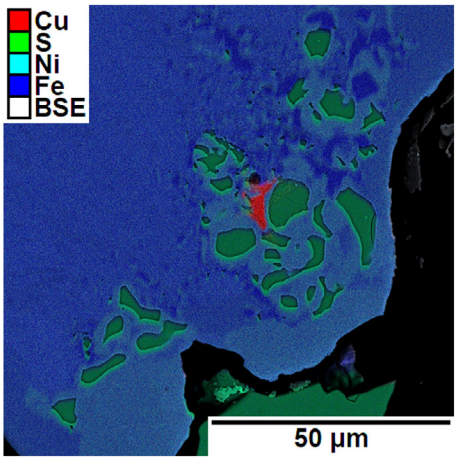

FIGURE 7. Metallic copper and irregular troilite in Sena. Image is a combined energy-dispersive spectroscopy (EDS) and backscatter electron (BSE) map of a subsection of the Sena thin section displaying both irregular troilite and metallic copper. Blue grain is Fe metal with varying Ni concentrations, green grains are troilite, and the red grain is Cu metal. Step size of the map is 34 nm, and beam settings were 1 nA and 15 kV. (Color figure can be viewed at wileyonlinelibrary.com.)

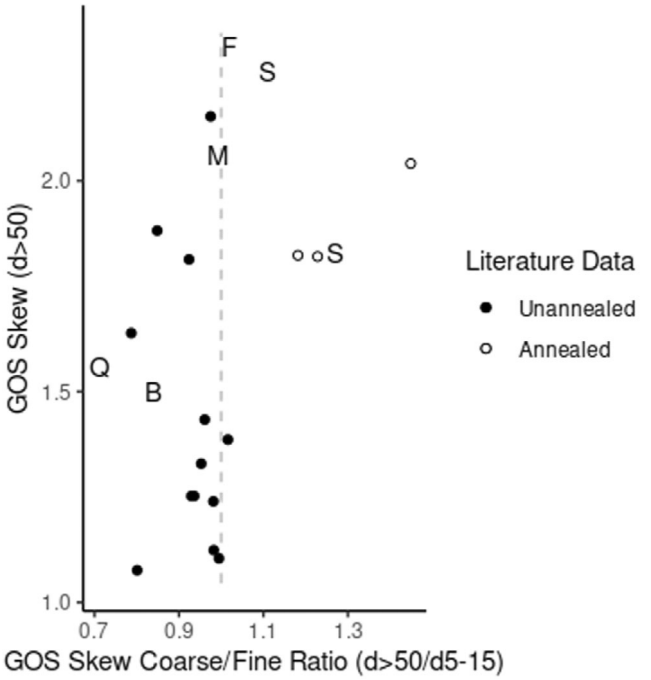

FIGURE 8. Grain orientation spread (GOS) skewness coarse/fine ratio parameter. Only coarse/fine ratio values elevated above proximity a value of 1 (gray-dashed line) are suggested to indicate annealing. Only our Sena sample ("S") meets this criterion. B is Beaver Creek, F is Forest Vale, Q is Quenggouk, M is Ste. Marguerite. Literature data are from Ruzicka and Hugo (2022a).

of olivine grains >50 µm (Figure 1), can be ambiguous in application as discussed earlier. Ruzicka and Hugo (2022a) propose a new technique for interpreting olivine EBSD data: the ratio between the GOS skewness of the olivine grain population with diameters >50 µm over that of the olivine grain population with diameters of 5–15 µm. The concept underlying this idea is that evidence of deformation is preferentially preserved in larger grains during annealing, so an elevated ratio in the skewness of coarse grains over that of fine grains could serve to indicate annealing (Figure 7). If this "coarse/fine ratio" is >1, then the data are interpreted as representing annealed samples. By this methodology, only our Sena sample qualifies as being annealed (Figure 8). However, we view this new technique and its implications with caution, especially since it implies that neither Quenggouk nor Beaver Creek is annealed, which contradicts previous TEM work (Ashworth, 1981). Ruzicka and Hugo (2022b) have also suggested that more precise deformational temperatures can be derived from the $f_{<010>} + f_{<001>}$ parameter, but applied to our samples, this technique does not provide temperature ranges (867–1099°C) that would disagree significantly with what we would have interpreted from the $f_{<010>} + f_{<001>}$ parameter.

CONCLUSIONS

In this study, we shed a new light on the impact history of the H chondrite parent body and the long-standing problem on whether it underwent thermal metamorphism as an undisturbed onion shell or was disrupted by a large impact. We did this by using EBSD microtectonic techniques on a selection of H4 samples that have been previously well examined by geochemical methodologies, microstructural techniques that are capable of revealing new information about these samples' histories. Our observations indicate that all samples have EBSD data consistent with a history of synmetamorphic shock and postshock annealing. The slow-cooled samples, Quenggouk and Sena, appear to have been subject to shock metamorphism without excavation during the process of thermal metamorphism, with adequate duration of elevated temperature afterward to allow annealing. The fast-cooled samples Beaver Creek, Forest Vale, and Ste. Marguerite also share this history of synmetamorphic shock and annealing, but were all excavated by impact(s) in the timeframe of 5.2–6.5 Ma post-CAI formation that exposed them to rapid cooling on the parent body surface. This collection of H4 sample histories is most consistent with a model of an intact, although impact-battered, onion shell parent body for <7.3 Ma post-CAI formation, but this does not rule out a later parent body disruption. Future work is needed, however, to see if these results are corroborated by similar methods applied to H5 and H6 chondrites, which are less sensitive to

surface impacting than H4 chondrites and are less likely to retain lingering accretion-related deformation.

Acknowledgments—We thank the editor, Christian Koeberl, and reviewers Alex Ruzicka and Alan Rubin for helpful feedback on this manuscript. We also appreciate Jasmeet Dhaliwal for helpful feedback on an early draft of this paper. We thank the Smithsonian for providing the meteorite samples used in this paper. This research was supported by the NASA Early Career Award to Myriam Telus and the University of California Cota-Robles Fellowship to Secana Goudy. Brendan Chapman was supported by the 2018 Summer Program in the Other Worlds Laboratory (OWL) at the University of California, Santa Cruz, a program funded by the Heising-Simons Foundation.

Data Availability Statement—Data available upon request from authors.

Editorial Handling—Dr. Christian Koeberl

REFERENCES

Archer, G. J., Walker, R. J., Tino, J., Blackburn, T., Kruijer, T. S., and Hellmann, J. L. 2019. Siderophile Element Constraints on the Thermal History of the H Chondrite Parent Body. *Geochimica et Cosmochimica Acta* 245: 556–76.

Ashworth, J. R. 1981. Fine Structure in H-Group Chondrites. *Proceedings of the Royal Society of London A* 374: 179–94.

Ashworth, J. R., and Mallinson, L. G. 1985. Transmission Electron Microscopy of L-Group Chondrites, 2. Experimentally Annealed Kyushu. *Earth and Planetary Science Letters* 73: 33–40.

Blackburn, T., Alexander, C. M. O'D., Carlson, R., and Elkins-Tanton, L. T. 2017. The Accretion and Impact History of the Ordinary Chondrite Parent Bodies. *Geochimica et Cosmochimica Acta* 200: 201–17.

Bouvier, A., Blichert-Toft, J., Moynier, F., Vervoort, J. D., and Albarède, F. 2007. Pb-Pb Dating Constraints on the Accretion and Cooling History of Chondrites. *Geochimica et Cosmochimica Acta* 71: 1583–604.

Ciesla, F. J., Davison, T. M., Collins, G. S., and O'Brien, D. P. 2013. Thermal Consequences of Impacts in the Early Solar System. *Meteoritics & Planetary Science* 48: 2559–76.

Davison, T. M., O'Brien, D. P., Ciesla, F. J., and Collins, G. S. 2013. The Early Impact Histories of Meteorite Parent Bodies. *Meteoritics & Planetary Science* 48: 1894–918.

Farla, R. J. M., Kokkonen, H., Fitzgerald, J. D., Barnhoorn, A., Faul, U. H., and Jackson, I. 2011. Dislocation Recovery in Fine-Grained Polycrystalline Olivine. *Physics and Chemistry of Minerals* 38: 363–77.

Friedrich, J. M., Ruzicka, A., Macke, R. J., Thostenson, J. O., Rudolph, R. A., Rivers, M. L., and Ebel, D. S. 2017. Relationships among Physical Properties as Indicators of High Temperature Deformation or Post-Shock Thermal Annealing in Ordinary Chondrites. *Geochimica et Cosmochimica Acta* 203: 157–74.

Ganguly, J., Tirone, M., Chakraborty, S., and Domanik, K. 2013. H-Chondrite Parent Asteroid: A Multistage Cooling, Fragmentation and Re-Accretion History Constrained by Thermometric Studies, Diffusion Kinetic Modeling and Geochronological Data. *Geochimica et Cosmochimica Acta* 105: 206–20.

Ganguly, J., Tirone, M., and Domanik, K. 2016. Cooling Rates of LL, L and H Chondrites and Constraints on the Duration of Peak Thermal Conditions: Diffusion Kinetic Modeling and Implications for Fragmentation of Asteroids and Impact Resetting of Petrologic Types. *Geochimica et Cosmochimica Acta* 192: 135–48.

Goetze, C., and Kohlstedt, D. L. 1973. Laboratory Study of Dislocation Climb and Diffusion in Olivine. *Journal of Geophysical Research* 78: 5961–71.

Goudy S. P. 2019. Assessment of Cluster Chondrite Accretion Temperature Using Electron Backscatter Diffraction and Implications for Chondrule Formation Models. Portland State University. http://meteorites.pdx.edu/pubs/Goudy2019-chondrite%20accretion%20temperature%20(PDX%20Scholar).pdf.

Guignard, J., and Toplis, M. J. 2015. Textural Properties of Iron-Rich Phases in H Ordinary Chondrites and Quantitative Links to the Degree of Thermal Metamorphism. *Geochimica et Cosmochimica Acta* 149: 46–63.

Harrison, K. P., and Grimm, R. E. 2010. Thermal Constraints on the Early History of the H-Chondrite Parent Body Reconsidered. *Geochimica et Cosmochimica Acta* 74: 5410–23.

Hellmann, J. L., Kruijer, T. S., Van Orman, J. A., Metzler, K., and Kleine, T. 2019. Hf-W Chronology of Ordinary Chondrites. *Geochimica et Cosmochimica Acta* 258: 290–309.

Henke, S., Gail, H. P., Trieloff, M., Schwarz, W. H., and Kleine, T. 2012. Thermal History Modelling of the H Chondrite Parent Body. *Astronomy and Astrophysics* 545: 1–15.

Hugo R. C., Ruzicka A. M., and Rubin A. E. 2019. Mesoscale and Microscale Shock Effects in the LL6 S4 Chondrites Saint-Séverin and Elbert: A Tale of Two Breccias. *Meteoritics & Planetary Science* 54, 1–21. https://doi.org/10.1111/maps.13304. Accessed September 14, 2022.

Huss, G. R., Rubin, A. E., and Grossman, J. N. 2006. Thermal Metamorphism in Chondrites. In *Meteorites and the Early Solar System II*, edited by D. S. Lauretta, and H. Y. J. McSween, 567–86. Tucson, AZ: University of Arizona Press.

Hutchison R. 1996. Hot Accretion of Ordinary Chondrites: The Rocks Don't Lie. Lunar and Planetary Science Institute 27, pp. 579–80.

Karato, S., and Ogawa, M. 1982. High-Pressure Recovery of Olivine: Implications for Creep Mechanisms and Creep Activation Volume. *Physics of the Earth and Planetary Interiors* 28: 102–17.

Karato, S., Jung, H., Katayama, I., and Skemer, P. 2008. Geodynamic Significance of Seismic Anisotropy of the Upper Mantle: New Insights from Laboratory Studies. *Annual Review of Earth and Planetary Sciences* 36: 59–95.

Kessel, R., Beckett, J. R., and Stolper, E. M. 2007. The Thermal History of Equilibrated Ordinary Chondrites and the Relationship between Textural Maturity and Temperature. *Geochimica et Cosmochimica Acta* 71: 1855–81.

de Kloe, R., Drury, M., and Farrer, J. K. 2002. Determination of Activated Slip Systems in Experimentally

Deformed Olivine-Orthopyroxene Polycrystals Using EBSD. *Microscopy and Microanalysis* 8: 680–1.
Lloyd, G. E., Farmer, A. B., and Mainprice, D. 1997. Misorientation Analysis and the Formation and Orientation of Subgrain and Grain Boundaries. *Tectonophysics* 279: 55–78.
Lucas, M. P., Dygert, N., Ren, J., Hesse, M. A., Miller, N. R., and McSween, H. Y. 2020. Evidence for Early Fragmentation-Reassembly of Ordinary Chondrite (H, L, and LL) Parent Bodies from REE-in-Two-Pyroxene Thermometry. *Geochimica et Cosmochimica Acta* 290: 366–90.
Metzler, K. 2012. Ultrarapid Chondrite Formation by Hot Chondrule Accretion? Evidence from Unequilibrated Ordinary Chondrites. *Meteoritics & Planetary Science* 47: 2193–217.
Monnereau, M., Toplis, M. J., Baratoux, D., and Guignard, J. 2013. Thermal History of the H-Chondrite Parent Body: Implications for Metamorphic Grade and Accretionary Timescales. *Geochimica et Cosmochimica Acta* 119: 302–21.
Prior, D. J., Boyle, A. P., Brenker, F., Cheadle, M. C., Day, A., Lopez, G., Peruzzi, L., et al. 1999. The Application of Electron Backscatter Diffraction and Orientation Contrast Imaging in the SEM to Textural Problems in Rocks. *American Mineralogist* 84: 1741–59.
Ream, M. T. 2019. *Geothermometry of H6 and L6 Chondrites and the Relationship between Impact Processing and Retrograde Metamorphism*. Portland State University. https://pdxscholar.library.pdx.edu/open_access_etds/5137/.
Rubin, A. E. 1994. Metallic Copper in Ordinary Chondrites. *Meteoritics* 29: 93–8.
Rubin, A. E. 2004. Postshock Annealing and Postannealing Shock in Equilibrated Ordinary Chondrites: Implications for the Thermal and Shock Histories of Chondritic Asteroids. *Geochimica et Cosmochimica Acta* 68: 673–89.
Ruzicka A. M., Goudy, S., and Hugo, R. C. 2020. Role of Hot Accretion and Deformation in Producing Cluster and Type 3 Ordinary Chondrites. 51st Lunar and Planetary Science Conference, abstract #1308.
Ruzicka, A., Hugo, R., and Hutson, M. 2015. Deformation and Thermal Histories of Ordinary Chondrites: Evidence for Post-Deformation Annealing and Syn-Metamorphic Shock. *Geochimica et Cosmochimica Acta* 163: 219–33.
Ruzicka, A. M., and Hugo, R. C. 2018. Electron Backscatter Diffraction (EBSD) Study of Seven Heavily Metamorphosed Chondrites: Deformation Systematics and Variations in Pre-Shock Temperature and Post-Shock Annealing. *Geochimica et Cosmochimica Acta* 234: 115–47.
Ruzicka, A. M., and Hugo, R. C. 2022a. A Robust Electron Backscatter Diffraction Annealing Metric for Olivine. 85th Annual Meeting of the Meteoritical Society, abstract #6179.
Ruzicka A. M., and Hugo, R. C. 2022b. Model Deformation Temperatures Derived from EBSD Data for Olivine in Type 6 Ordinary Chondrites and Ureilites. 53rd Lunar and Planetary Science Conference, abstract #1757.
Scott, E. R. D., Krot, T. V., Goldstein, J. I., and Wakita, S. 2014. Thermal and Impact History of the H Chondrite Parent Asteroid During Metamorphism: Constraints from Metallic Fe-Ni. *Geochimica et Cosmochimica Acta* 136: 13–37.
Stöffler, D., Keil, K., and Scott, E. R. D. 1991. Shock Metamorphism of Ordinary Chondrites. *Geochimica et Cosmochimica Acta* 55: 3845–67.
Stöffler, D., Keil, K., and Scott, E. R. D. 1992. Shock Classification of Ordinary Chondrites: New Data and Interpretations. *Meteoritics* 27: 292–3.
Stöffler, D., Hamann, C., and Metzler, K. 2018. Shock Metamorphism of Planetary Silicate Rocks and Sediments: Proposal for an Updated Classification System. *Meteoritics & Planetary Science* 53: 5–49.
Taylor, J. G., Maggiore, P., Scott, E. R. D., Rubin, A. E., and Keil, K. 1987. Original Structures, and Fragmentation and Reassembly Histories of Asteroids: Evidence from Meteorites. *Icarus* 69: 1–13.
Telus, M., Huss, G. R., Nagashima, K., and Ogliore, R. C. 2014. Revisiting ^{26}Al-^{26}Mg Systematics of Plagioclase in H4 Chondrites. *Meteoritics & Planetary Science* 49: 929–45.
Toriumi, M., and Karato, S. 1978. Experimental Studies on the Recovery Process of Deformed Olivines and the Mechanical State of the Upper Mantle. *Tectonophysics* 49: 79–95.
Trieloff, M., Jessberger, E. K., Herrwerth, I., Hopp, J., Flénl, C., Ghélis, M., Bourot-Denise, M., and Pellas, P. 2003. Structure and Thermal History of the H-Chondrite Parent Asteroid Revealed by Thermochronometry. *Nature* 422: 502–6.
Zinner, E., and Göpel, C. 2002. Aluminum-26 in H4 Chondrites: Implications for its Production and its Usefulness as a Fine-Scale Chronometer for Early Solar System Events. *Meteoritics & Planetary Science* 37: 1001–13.

SUPPORTING INFORMATION

Additional supporting information may be found in the online version of this article.

Figure S1. GROD map of Beaver Creek thin section.

Figure S2. GROD map of Forest Vale thin section.

Figure S3. GROD map Quenggouk thin section.

Figure S4. GROD map of Sena thin section (2 μm step size).

Figure S5. GROD map of Ste. Marguerite thin section.

Figure S6. GROD map of Sena thin section (4 μm step size).